

Research Article

Crosswise Wind Shear Represented as a Ramped Velocity Profile Impacting a Forward-Moving Aircraft

Mahmood Khalid 

Department of Aeronautical Engineering, King Abdulaziz University, Jeddah 21589, Saudi Arabia

Correspondence should be addressed to Mahmood Khalid; mkholid@kau.edu.sa

Received 12 December 2018; Accepted 27 February 2019; Published 18 August 2019

Academic Editor: Linda L. Vahala

Copyright © 2019 Mahmood Khalid. This is an open access article distributed under the Creative Commons Attribution License, which permits unrestricted use, distribution, and reproduction in any medium, provided the original work is properly cited.

Abrupt changes in wind velocities over small distances in a lateral or vertical direction can produce wind shear which is known to have serious effects upon the performance of an aircraft. Brought about by large-scale changes in the atmospheric conditions, it is a three-dimensional flow phenomenon imposing severe velocity gradients on an aircraft from all possible directions. While it would be difficult to model an instantaneous velocity gradient in a lateral plane, a vortical flow impinging from the sides which represents a wind shear in a vertical direction is imposed on a forward-moving aircraft to investigate the effect on the aerodynamic performance. The maximum shear wind speed from the side was fixed at 0.3 times the forward velocity. After due validations under no-wind shear conditions on simpler half-reflection plane models, a BGK airfoil-based full 3D wing and the ONERA M6 3D wing model were selected for preliminary studies. The investigation was concluded using the ARA M100 wing-fuselage model.

1. Introduction

There are large numbers of weather patterns which can produce sudden three-dimensional uneven flow conditions anywhere in the atmosphere. Horizontal wind shearing gradients are generally produced when masses of air move between different weather fronts at different temperature pressures and humidity. The wind shear will be present at the boundaries of these fronts. Severe weather conditions include thunderstorms which often contain tornadoes and hailstorms energized by wind shear. The large-scale flow circulation within the same system brought about by large temperature and pressure differences produces downbursts as shown in Figure 1.

Figure 1 shows a massive downward movement of high-energy winds which spread out in all directions at the bottom end. An aircraft moving through such shear winds will have to contend with sharp wind gradients in both lateral and vertical directions. A shearing wind in a forward planar sense would tempt the pilot to reduce the speed as the vehicle maintains a constant Mach number entering a strong front and thus loose height. With subsequent tail wind, the aircraft would speed up to maintain a constant Mach number. The

recovery might be too late. It is important to note that shear winds can occur at any altitude with little time for the aircraft to recover at lower altitudes. There are several aircraft crashes attributed to wind shear. From 1964 to 1985, wind shear directly caused or contributed to 26 major civil transport aircraft accidents in the U.S. that led to 620 deaths and 200 injuries. Following such numerous mishaps in the 1970's and 80's, the FAA in US stipulated [1] that all commercial aircraft must be equipped with an on-board wind shear detection system, and the same body has initiated concerted research programs [2, 3] to safeguard against wind shear problems.

Understanding the implications of wind shear following a microburst phenomenon upon aircraft performance has been a challenge for aircraft designers, pilots, and the aviation control authorities. Frost [4] has documented the extent of these challenges by studying the nature of such wind shear fronts from thunderstorms, the computer modeling of the wind shear phenomenon, ground-based and airborne detection systems, the governing equations which control the automatic aircraft response, the pilot's control of the aircraft in such nonuniform environment, and the avoidance and safety procedures for worst possible scenarios during take-off and landing. In terms of horizontal shear wind velocity



FIGURE 1: NASA picture of a microburst over an airport runway.

components from downbursts, Fujita and Wakimoto [5] show Doppler measurements of 30 m/s at altitudes less than 200 m which can be extremely dangerous during take-off and landing. Mulgund and Stengel [6] have provided a sinusoidal F -factor variation of the microburst from extreme intensity at 0 location to a ± 7500 m range. The shear component at a maximum velocity of 110 m/s can drop from 45 m/s to about -2 m/s.

Simulating the effects of atmospheric turbulence using LES or DNS according to Jameson and Fatica [7] is a daunting prospect where the eddy length scales can be as low as $1/Re^{3/4}$ of a macroscopic length and a CFD simulation of a commercial airplane may require as many as $Re^{9/4}$ cells. Moin and Kim [8] on the other hand estimate that an airliner with a 50 m long fuselage cruising at 250 m/s at a height of 10000 m would require 10^{16} million points to simulate turbulence near the surface with any reasonable detail. It is further estimated that with 1 tera-flop performance, it would take a computer 1000 years to simulate 1 second of that flight! Spalart et al.'s earlier projections [9] seemed more optimistic which stated that based on the current rate of progress, DNS-based simulation on a complete aircraft would be possible by 2075.

The present investigation concentrates upon a simplified model of the wind shear in the vertical direction where a rotational side shear flow is imposed as the aircraft with uniform forward velocity. The DNS-based simulations of the true wind shear even on a simple 3D tapered wing are still beyond the practicalities of available computational horse power. The flow topology model is shown in Figure 2. In essence, a vorticity vector is imposed from one side of a forward-moving aircraft. The vorticity vector has a maximum velocity at the top end reducing to zero at

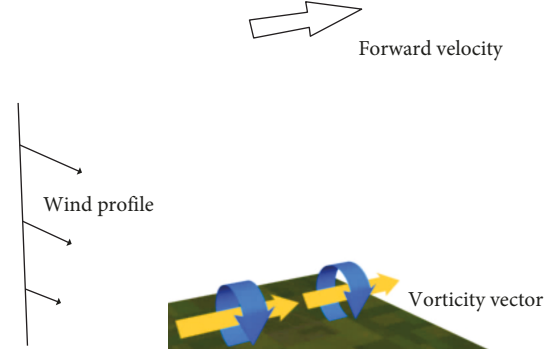


FIGURE 2: Velocity vectors imposed upon an aircraft in steady flight.

the plane of the aircraft and then increases negatively in the other direction to a maximum at the same distance below the aircraft.

Three separate models were investigated in the course of the present study. The first was a theoretical 3D swept and tapered model constructed from the BGK airfoil used in well-known wind tunnel-based experimental programs at IAR/NRC (Canada) and NLR (Japan) as contained in Plo-senski et al. [10] and Sudani et al. [11], respectively. The second of the three models was configured from the ONERA M6 model as described in the AGARD-based wind tunnel experimental study by Schmitt and Charpin [12]. The third model, the ARA M100 model from Carr and Pallister [13], was selected to include the effects on the fuselage from the side shear.

The first phase of the study involved the computational validation for the three models. The flow past all 3D models was first studied under normal forward flow conditions, and the results were compared against measurements carried out in various wind tunnels. After due validation, a vertical shear flow which varied from a maximum lateral flow at the top of the grid to zero in the aircraft horizontal plane to a negative maximum at the bottom end of the mesh was imposed upon the normal forward flow condition. The side vortical flow appears to degrade the aerodynamic performance of the aircraft.

2. Computational Program

It would be appropriate to provide some comments on the computational algorithm used for the present work. The conservative form of the compressible Reynolds-averaged Navier-Stokes equations in the index form is given as follows:

$$\begin{aligned} \frac{\partial \rho}{\partial t} + \frac{\partial(\rho u_i)}{\partial x_i} &= 0, \\ \frac{\partial(\rho u_i)}{\partial t} + \frac{\partial}{\partial x_j} \left[\rho u_i u_j + p \delta_{ij} - \left(1 + \frac{\mu_t}{\mu} \right) \tau_{ij} \right] &= 0, \\ \frac{\partial(\rho E)}{\partial t} + \frac{\partial}{\partial x_j} \left[\rho u_j E + u_j p - \left(1 + \frac{\mu_t}{\mu} \right) u_i \tau_{ij} - \left(c_p \frac{\mu}{Pr} + c_p \frac{\mu_t}{Pr_t} \right) \frac{\partial T}{\partial x_j} \right] &= 0, \end{aligned} \quad (1)$$

where ρ in these equations refers to the density, p to pressure, and T to temperature; E is the total energy; and u is the velocity vector in tensor format. τ_{ij} is the viscous stress tensor which may be written as

$$\tau_{ij} = \mu \left(\frac{\partial u_i}{\partial x_j} + \frac{\partial u_j}{\partial x_i} - \frac{2}{3} \frac{\partial u_k}{\partial x_k} \delta_{ij} \right). \quad (2)$$

The above Navier-Stokes equations, formulated in strong conservation form to be used in the structured meshes of the present study, are first cast into a curvilinear coordinate scheme following the Vinokur [14] transformation method. The numerical algorithm used to solve the Navier-Stokes equations is an implicit factorization finite centre difference scheme about a regular rectangular prism which is described at length by Beam and Warming [15]. Local time linearization is applied to the nonlinear terms following Pulliam and Chaussee [16]. An approximate factorization scheme is applied to the resulting matrices which factorizes the operator itself resulting in efficient matrix equations with narrow bandwidth. This results in block tridiagonal matrices which are easy to solve. The spatial derivatives can thus be approximated using second-order central differences. Explicit and implicit artificial dissipation terms are added to achieve nonlinear stability. A spatially variable time step is used to accelerate convergence to steady state solutions. The algorithm can be used to solve time accurate or steady state flow problems.

While the present study was not meant to scrutinize the accuracies of various turbulence models, still, some preliminary calculations were conducted using both the one-equation, Baldwin and Barth [17] and the Spalart and Allmaras [18] turbulence models, and the two-equation $k-\epsilon$ and $k-\omega$ turbulence models to assure that the application of the selected turbulence model would provide reasonably accurate results. The intention was to understand the global effects on the performance of an aircraft as a result of strong side shear winds rather than analyzing the precision of a certain finding.

3. Simulating the Microburst

The microburst occurring at some altitude in a simplified model as shown in Figure 1 forces an axisymmetric 3D jet downwards which spreads out as it moves towards denser atmospheric layers and finally folds backward and outwards like a bell as it reaches stagnation conditions. It is appropriate to estimate the velocity components from the simple microburst model shown in Figure 3.

Using the stream function, we can write the u and v components of velocities in the downburst as

$$\begin{aligned} u &= -\frac{1}{x} \frac{\partial \psi}{\partial y}, \\ v &= \frac{1}{x} \frac{\partial \psi}{\partial x}, \end{aligned} \quad (3)$$

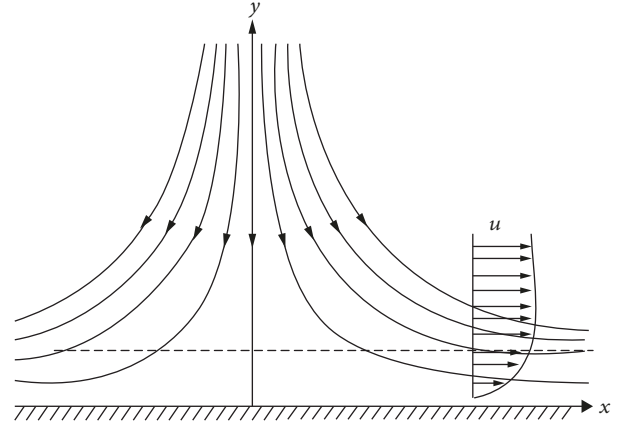


FIGURE 3: Axisymmetric downburst.

which can in turn be substituted back into the radial equation where coordinate x now defines the radial parameter:

$$u \frac{\partial u}{\partial x} + v \frac{\partial u}{\partial y} = -\frac{1}{\rho} \frac{\partial p}{\partial x} + \nu \left[\frac{1}{x} \frac{\partial}{\partial x} \left(x \frac{\partial u}{\partial x} - \frac{u}{x^2} + \frac{\partial^2 u}{\partial^2 y^2} \right) \right]. \quad (4)$$

The stream function in an inviscid simplified model as we approach the axisymmetric stagnation point is given by

$$\psi = -Bx^2y, \quad (5)$$

where the velocity components u and v now become

$$\begin{aligned} u &= Bx, \\ v &= -2By. \end{aligned} \quad (6)$$

Making use of the Homann [19] nondimension variable for the axisymmetric flow, we have

$$\begin{aligned} \eta &= y \sqrt{\frac{B}{\nu}}, \\ \psi &= -x^2 F(\eta) \sqrt{B\nu}, \end{aligned} \quad (7)$$

which now enable us to express u and v in a dimensionless form as

$$\begin{aligned} u &= Bx F'(\eta), \\ v &= -2F(\eta) \sqrt{B\nu}. \end{aligned} \quad (8)$$

The radial momentum in the x axisymmetric direction now becomes

$$F''' + 2FF'' + 1 - F'^2 = 0. \quad (9)$$

Using the boundary conditions $F(0) = F'(0) = 0$ and $F(\infty) = 1$, the above equation can be solved with the Runge-Kutta differential scheme. Figure 4 shows a typical solution.

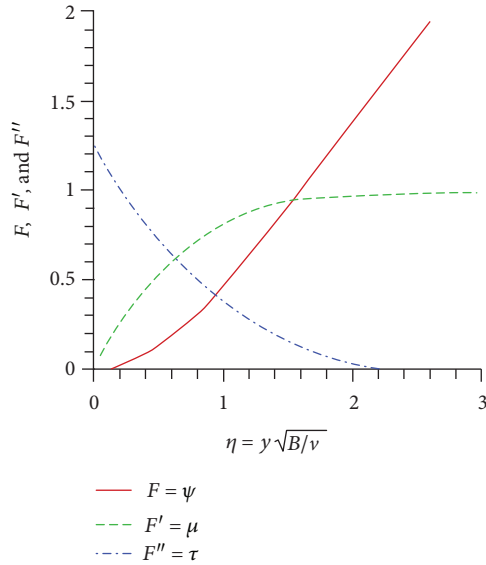


FIGURE 4: Axisymmetric downburst against ground-velocity solution.

Figure 4 shows how the two components of velocities u and v change with η . The downburst contains high-velocity winds at altitude which convert more towards a horizontal velocity component at lower altitude as the downburst spreads out horizontally. Gusty winds from such thunderstorms and downdrafts spread out quickly and forcefully. These winds according to FAA [20] can reach 100 knots and change the direction by as much as 180° as early as 16 km ahead of the storm itself. The gust wind speeds can suddenly increase by as much as 50% within 450 m with maximum speeds within the first 45 m. In our simple side shear model, we have given the maximum shear speed to be about 30% of the aircraft forward velocity. The maximum speed was being ramped from -30% at the bottom plane to 30% at the other end. The distance between maximum velocities was varied from about 4 m to 25 m. A more comprehensive simulation might investigate the parallel effect of a sinusoidal side gust wind or even a lateral variation of maximum speed from one spanwise location to a minimum or even negative at the other spanwise location.

4. Simulating the Flow Past Aerodynamic Models

4.1. Aerodynamic Performance of the BGK Wing. A BGK airfoil was first used to construct a wing having a constant chord length and placed in a wind tunnel used for 2D testing. The mesh used for this planar 2D wind tunnel model is shown in Figure 5.

The validation study involved computations at two flow conditions: $M = 0.496$, $\alpha = 5.63^\circ$ and $M = 0.738$ and $\alpha = 3.52^\circ$. Two meshes of similar overall dimensions of $163 \times 65 \times 25$ but with y^+ value for the first mesh line of 1~2 and 3~4 were tried. Figure 6 shows the comparison of the surface pressure distribution on this 2D wing at

the lower Mach number of $M = 0.496$ and angle of attack $\alpha = 5.63^\circ$.

All the turbulence models have performed well in resolving the surface pressure distribution. It appears that at least at this lower Mach number of $M = 0.496$, there is no great benefit in using a higher-order turbulence model. The pressure distribution results for the higher Mach number of $M = 0.738$ and $\alpha = 3.52^\circ$ are shown in Figure 7.

The results for the Spalart and Allmaras model could not be shown as the algorithm seemed to blow up as soon as the computations were switched from a basic algebraic model to the higher-order turbulence model after the first preliminary 100 iterations. These procedures of initiating with a lower-order turbulence model and then switching to the two-equation model were adapted for most higher-order turbulence models. It is noted from the pressure distribution in this case that all turbulence models performed well in predicting the overall pressure distribution on both top and bottom surfaces; however, the one-equation Baldwin and Barth model with the first mesh line having a value of $y^+ 1\sim 2$ performed much better in the placement of the shock location compared to other computations. The Baldwin and Barth being the one-equation turbulence model and the cheapest to run was the code used in subsequent computations.

The lift and drag coefficients for the above two cases with the Baldwin and Barth case using a mesh of $y^+ 1\sim 2$ at the first grid line were duly calculated and compared against the experiment. The values are shown in Table 1.

4.2. BGK Wing under Side Wing Shear. The next step in this study was to study a simple 3D wing configuration joined at the point of symmetry with an identical reflection plane wing without a fuselage in between. The 3D wing was constructed with the BGK airfoil coordinates with a root chord length of 1 m which narrowed to a tip chord length of 0.56 m, with a wing semispan of 1.476 m. Its leading edge swept at an angle of 60° , and the trailing edge sweep was 72.17° . The 3D wing under no-applied side shear wind colored by pressure contours is shown in Figure 8. It stood aloof from the walls with a tip mesh which separated the solid from the far boundary as shown in Figure 8. The complete mesh consisted of $163 \times 65 \times 77$ dimensions with 14 grid lines from each of the two spanwise boundaries reserved for the tip mesh supporting the model at both ends.

An extended version of this wing was also examined in order to study the folding tips or winglets from the oncoming side wind shear. A simple wing tip was constructed with a chord length of $1/4^{\text{th}}$ of the root chord length and placed at the station 1.62 m from the root chord with the leading edge in line with the tip of the main plain wing. Thus, its inward angle was set at 39.8° to the main wing plane. Figure 8 shows this wing with a wingtip under side shear. Figure 9 shows the same wing equipped with a folding winglet-type tip.

A side wind shear as depicted in Figure 3 was now applied from the starboard side. This side wind shear reached a maximum of 0.3 times the forward velocity in a direction from the starboard side at the top of the mesh, which is 25 m above the plane of the 3D wing, and decreased proportionately with

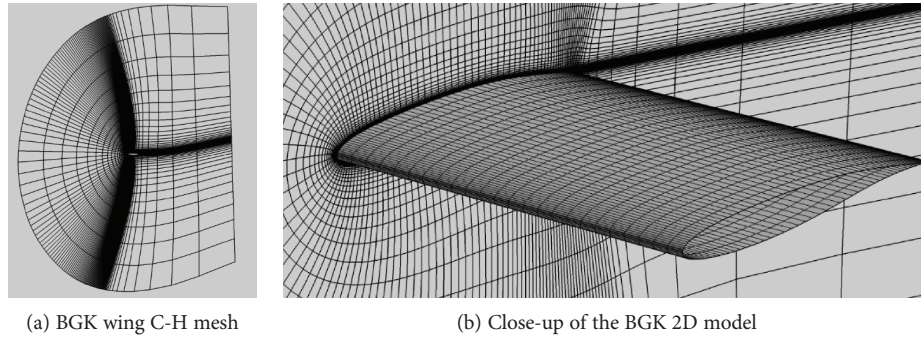


FIGURE 5: 2D planar BGK wing.

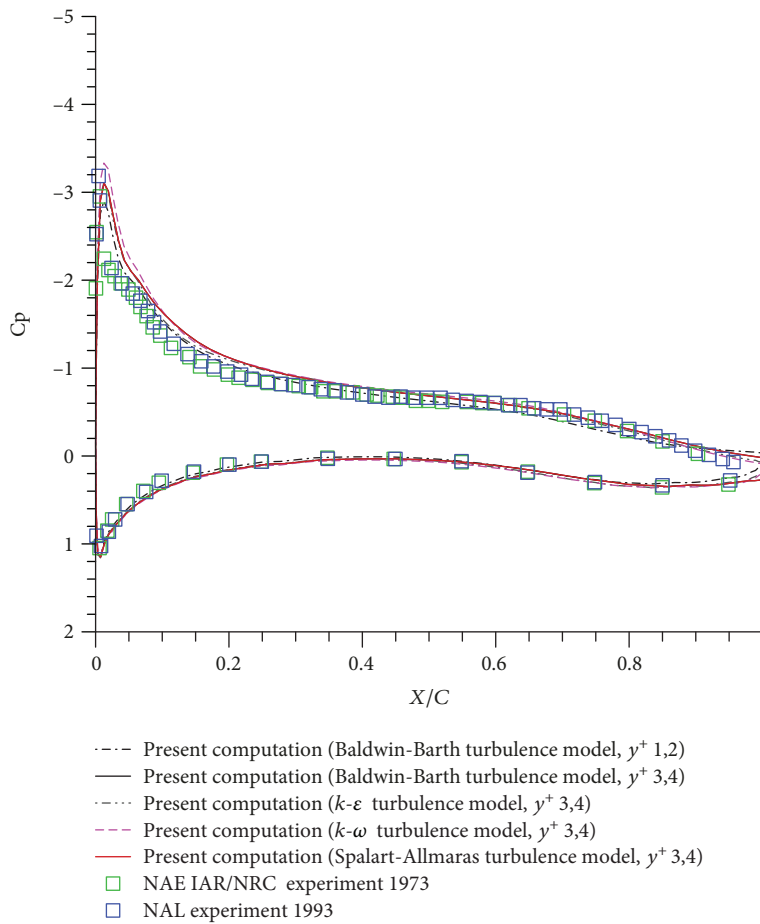


FIGURE 6: Pressure distribution at $M = 0.496$ and angle of attack $\alpha = 5.63^\circ$.

the height of the mesh line, reaching a zero velocity in the wing plane. It then increased negatively in the downward direction reaching a maximum of 0.3 times the forward velocity towards the starboard direction. Figure 10(a) shows this side wind shear (SW1) at the starboard side far boundary. Figure 10(b) shows the same side wind shear (SW2) when the distance between the positive and the negative maximum velocities was reduced to 10 m.

The solution as observed in Figure 10(c) converged quite satisfactorily to at least 2 orders of magnitude as shown by the drop in L2 residual within 2500 iterations. L2 in present

computations measures an average of the maximum of all the variables used in the Navier-Stokes equations. It has been confirmed by monitoring other loads and moments on the wing that a drop of at least 2 orders of magnitude leads to reasonably well-converged solutions. The pressure distributions on the surface were suitably integrated along with the surface skin friction to arrive at the wing lift and drag coefficient. Figure 11 shows streamlines past the BGK wing with and without a folding wing tip in a steady flow with no shear. Figure 12 is effectively a close-up view of Figure 11(a), while Figures 13 and 14,

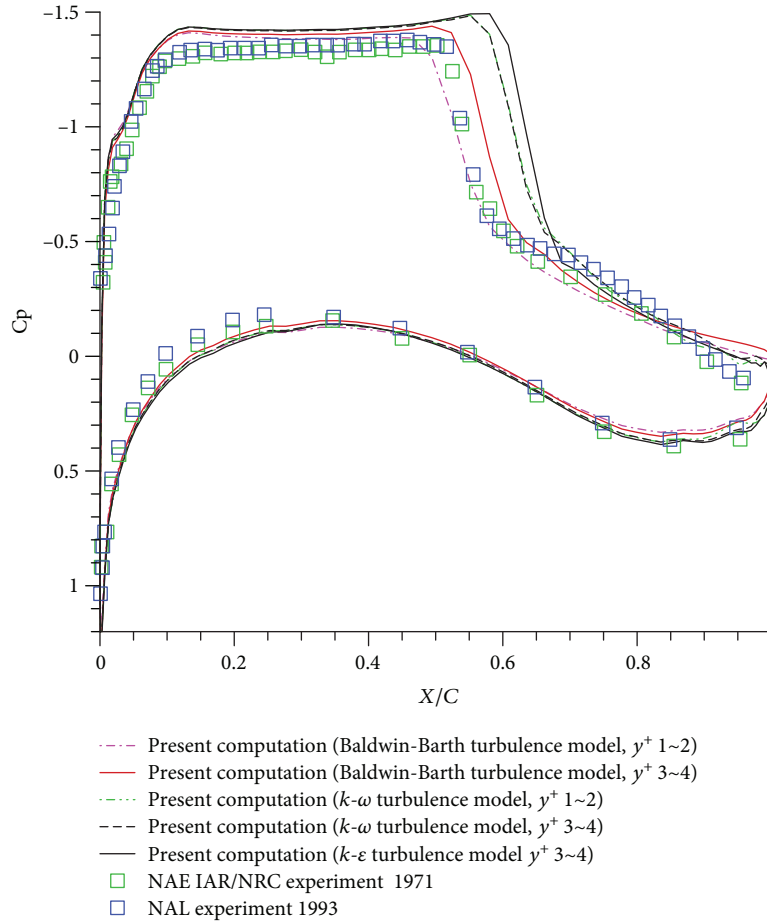


FIGURE 7: Pressure distribution at $M = 0.738$ and angle of attack $\alpha = 3.52^\circ$.

TABLE 1: Lift and drag coefficient comparisons.

Test type	NAL $M = 0.496$, $\alpha = 5.73^\circ$ IAR/NRC $M = 0.496$, $\alpha = 5.76^\circ$ $Re = 20 \times 10^6$		NAL $M = 0.738$, $\alpha = 3.52^\circ$ IAR/NRC $M = 0.738$, $\alpha = 3.67^\circ$ $Re = 20 \times 10^6$	
	C_L	C_D	C_L	C_D
	Experiment	0.917 0.906	0.0079 0.0079	0.886 0.896
Computation	0.915	0.0099	0.924	0.0222

respectively, show the same two wings with side wind shears as depicted in Figures 10(a) and 10(b).

It is noted especially when the maximum shearing velocity is close to the wing (SW2) that the streamlines passing along the portside wing tip are bent inwards towards the centre line. It also appears that the effect of folding wing tips on the presence of the side wind shear modifies the pressure distribution at the leading edge of the wing. Streamlines passing close to the wing tips of a folded wing tip as seen in Figures 15 and 16 are bent differently as the flow field responds to SW1 and SW2. The streamlines under wind shear SW2 bend more inwardly towards the centre. Table 2 has been provided to quantify the effects of actual loads on the wing as a result of the side wind shear with and without the folding wing tips.

The lift and drag coefficient as itemized in Table 2 shows that lift tends to increase while there is a decrease in drag when the maximum velocities of the shearing wind are more distant from the plane of both types of the wing. For the plain wing, there is a noticeable decrease in lift accompanied with drag rise when the maximum shear velocities are closer to the wing plane. For the wing with a folding wing tip, the lift to drag coefficient shows that there would be a sudden rise in C_L/C_D when the maximum shearing velocities are more distant from the wing plane.

4.3. ONERA M6 Wing under Side Shear Winds. The next model selected to further probe the behaviour of wings under side wind shear was the ONERA M6 wing. This is a well-recognized wing in the aerodynamic community, and many

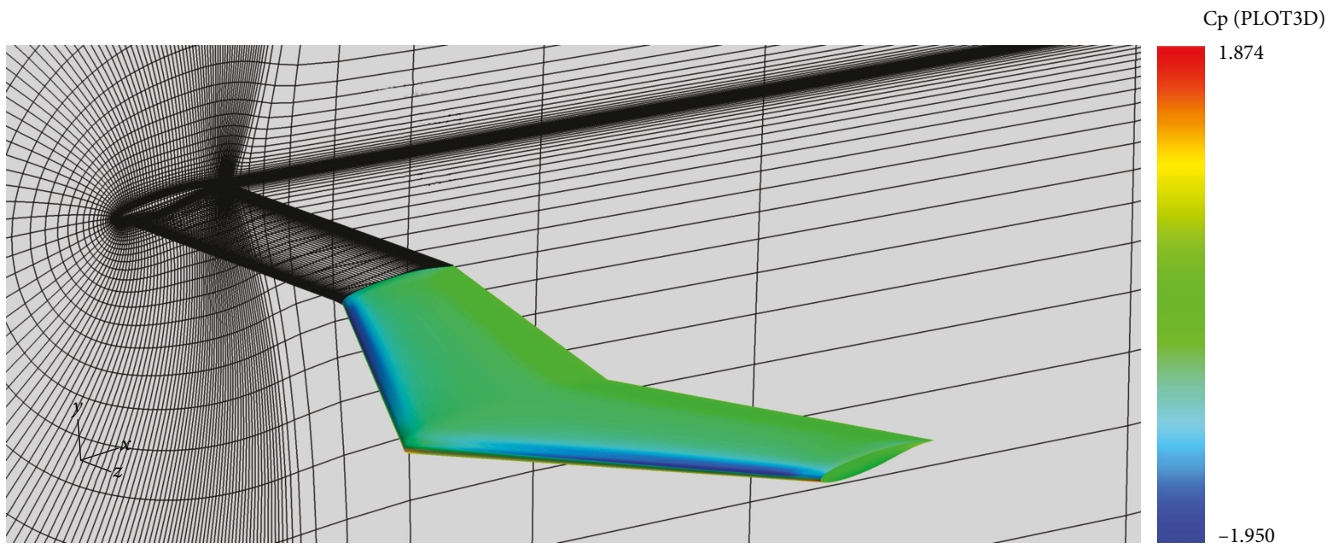


FIGURE 8: The plain 3D wing constructed from the BGK airfoil.

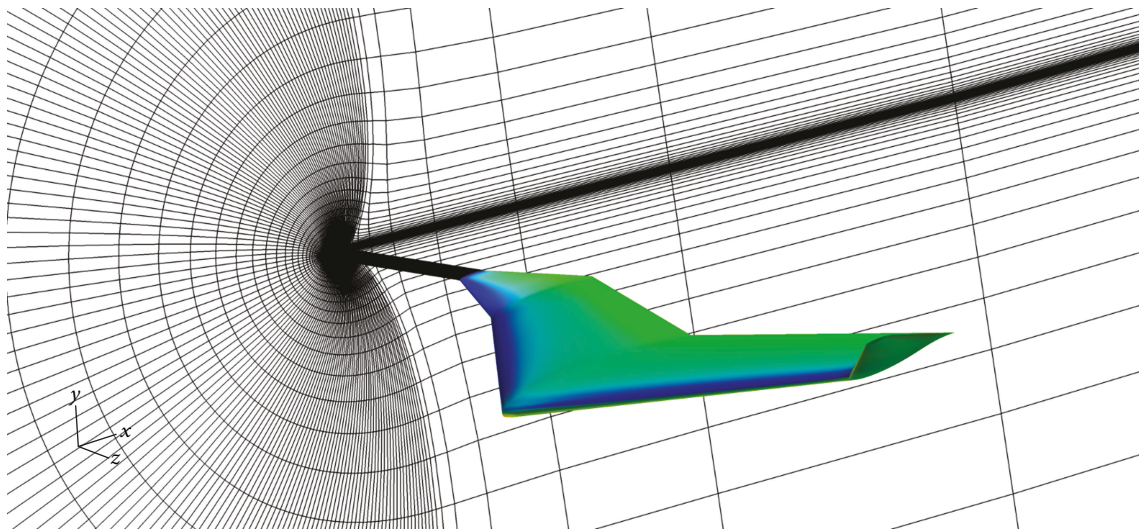


FIGURE 9: The 3D wing with folding tips constructed from the BGK airfoil.

concept-proving studies have been carried out using this wing. Figure 17 shows this ONERA M6 wing encapsulated in the mesh which was used to study this wing. The pressure on the wing was calculated at the standard Mach number of $M = 0.84$ and $\alpha = 3.06^\circ$. The mesh once again contained 163 points in the chordwise direction while 14 points separated the wing tip from the spanwise far boundary leaving 25 spanwise points on the actual wing surface. The first mesh line was placed at 0.00002 units off the surface with 65 grid points in the normal direction giving a y^+ value of 3~4 for the first mesh point around the wing periphery.

The pressure distributions as contained in Figure 18 were obtained at 3 locations: two of which were selected near the wing root and the third chosen nearest to the tip. The results show that the computational algorithm performs satisfactorily for this model. As no measured lift and drag loads are available from the experiment from Schmitt and Charpin

[12], the integrated lift and drag on this model were compared against similar computations from Durrani and Qin [21] which also contained results from Le Moigne [22], Neilsen and Anderson [23], and Lee et al. [24]. The comparison is shown in Table 3. The results are consistent with findings from other researchers.

As a next step, again, the side wind shear was applied to this plane wing with and without the folding tip copied from the previous BGK wing. Figure 19 shows the streamlines under the influence of the side wind shear near the ONERA M6 complete wing with and without the presence of the conceptual folding tip.

The streamlines in Figure 20(a) show that there is a very noticeable twisting of the streamlines from the presence of the folding tips on the ONERA M6 wing. Note that as depicted in Figure 20(b), the solution converged by a good 2 orders of magnitude within the first 25 iterations. Beyond

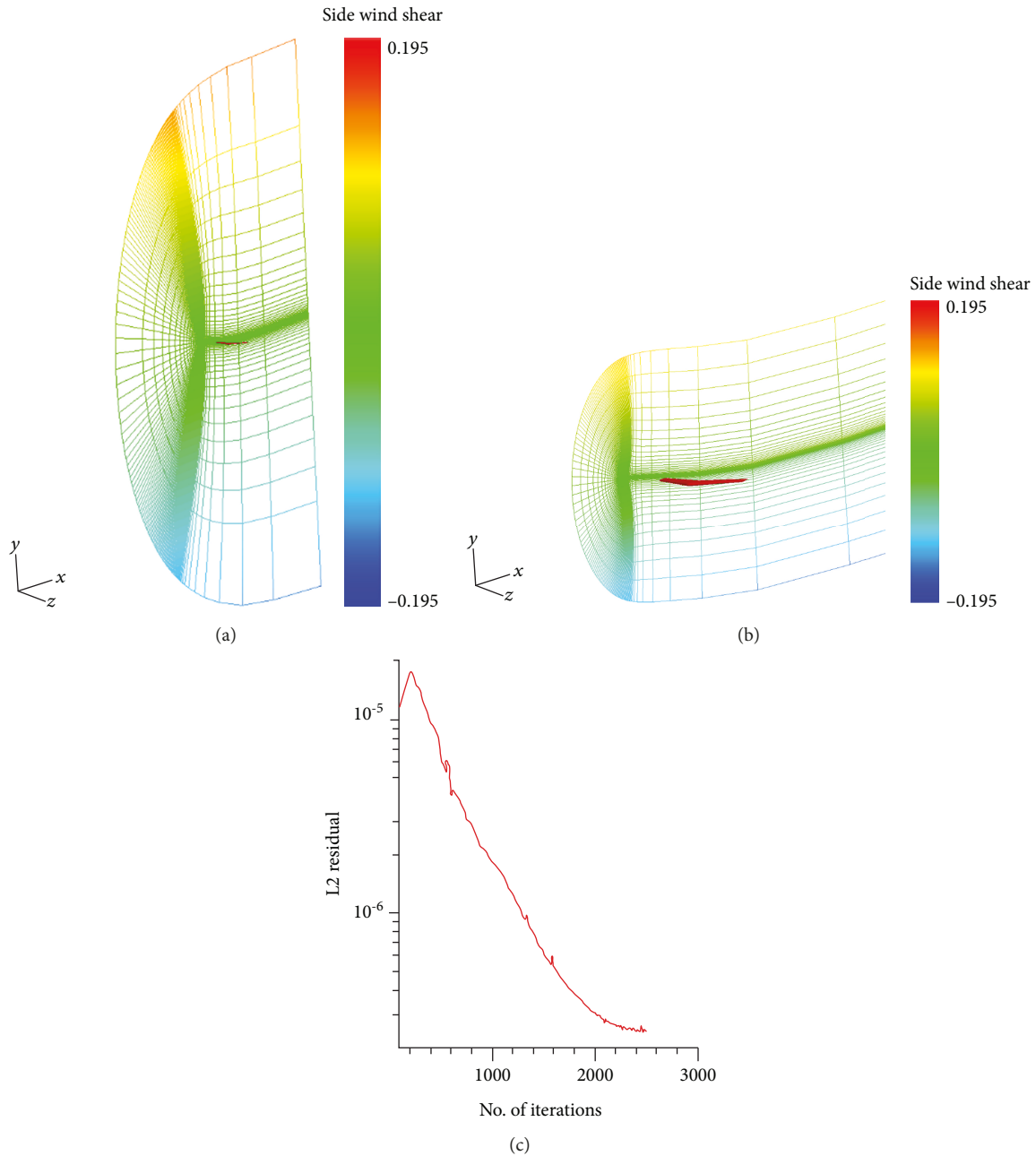


FIGURE 10: Wind shear at the far starboard boundary with the 3D wing in the centre.

this point, the solution just oscillates within a very small margin of amplitude. More definitive aerodynamic performance can be assessed from the tabulated lift and drag data when compared against the plain wing with no-wind shear (Table 4).

It is clear that as for the BGK conceptual wing studies earlier, the wing with the folding tip would respond most vigorously to the side wind shear. The side wing loads on the vertical tail; and rudder under side wind shear condition would also be more sensitive to such conditions.

4.4. ARA M100 Wing-Fuselage Configuration Studies. The ARA M100 wing with a fuselage was the next model to be studied under side wind shear loads. Since it was the first

model containing a fuselage geometry which was likely to interfere more with the side shear winds, it was expected to be more responsive to interfering cross loads. At first, two flow conditions from the experiment were selected to verify the quality of flow predictions from the present algorithm. These two flow conditions were $M = 0.8027$, $\alpha = 2.873^\circ$, and $Re/m = 13 \times 10^6$ and $M = 0.6$, $\alpha = 1.733^\circ$, and $Re/m = 13 \times 10^6$. Figure 21 shows basic dimensions of the ARA M100 model, and Figure 22 displays the reflection plane M100 model along with the model support encapsulated with the mesh used to compute the flow. Surface pressure distribution for the first flow conditions $M = 0.8027$, $\alpha = 2.873^\circ$, and $Re/m = 13 \times 10^6$ for the complete model is shown in

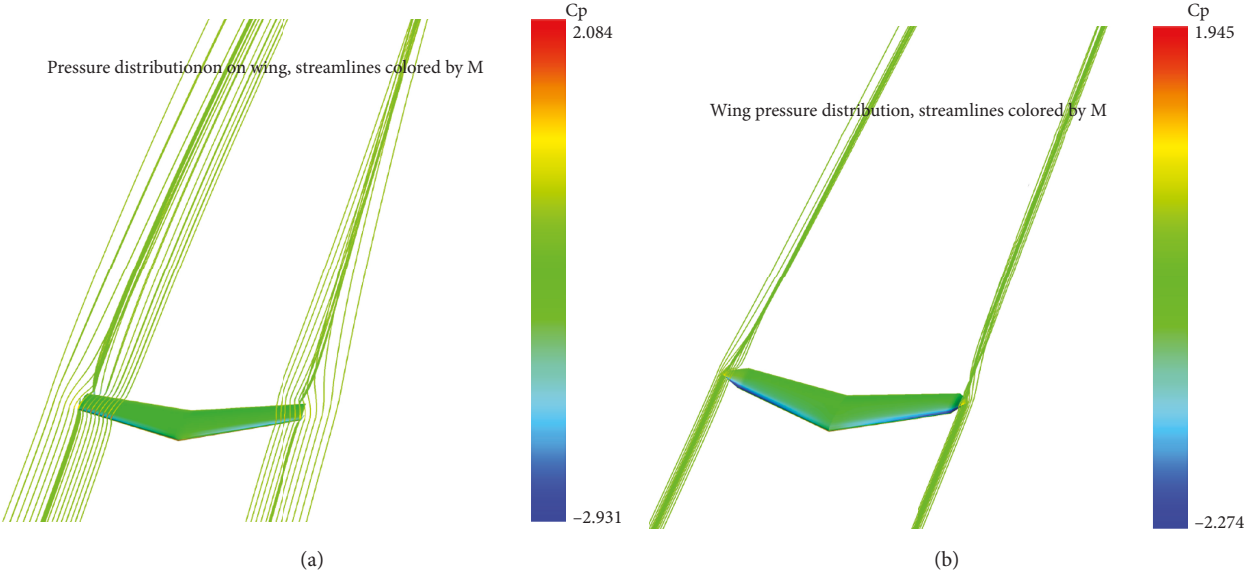


FIGURE 11: Plain BGK wing (a) and with folding tips (b) under no side wind shear.



FIGURE 12: BGK wing under no side wind shear.

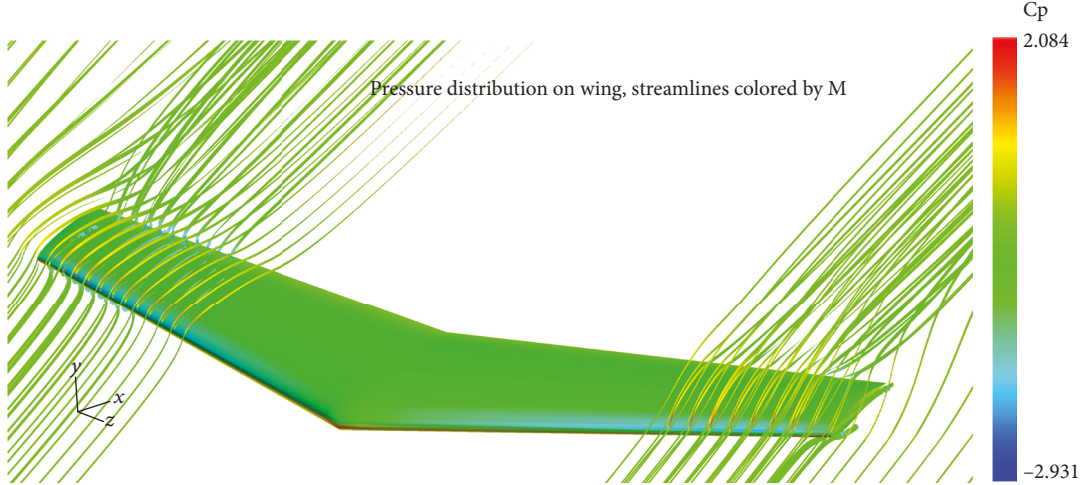


FIGURE 13: BGK wing under side wind shear (SW1).

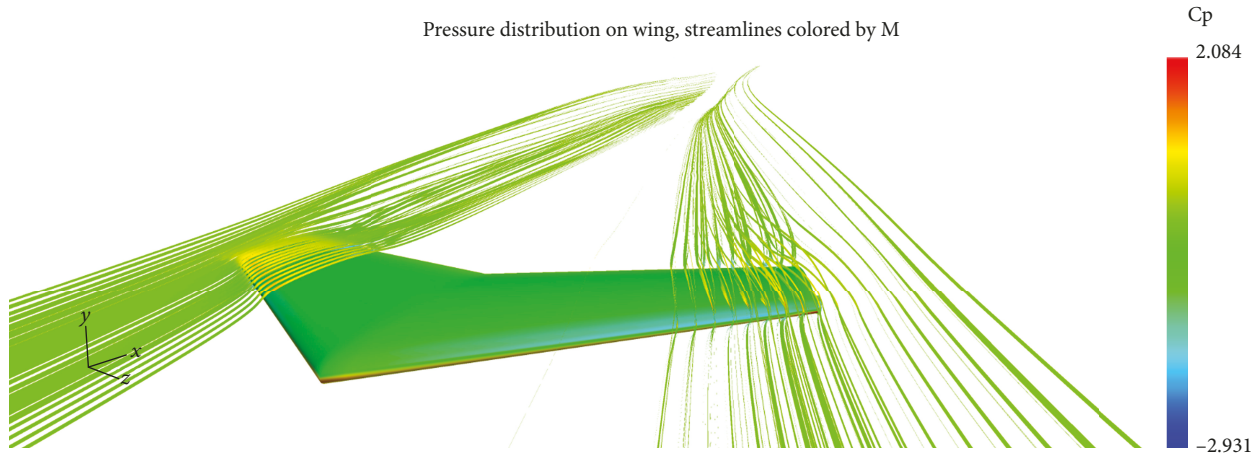


FIGURE 14: Plain BGK wing under side wind shear (SW2).

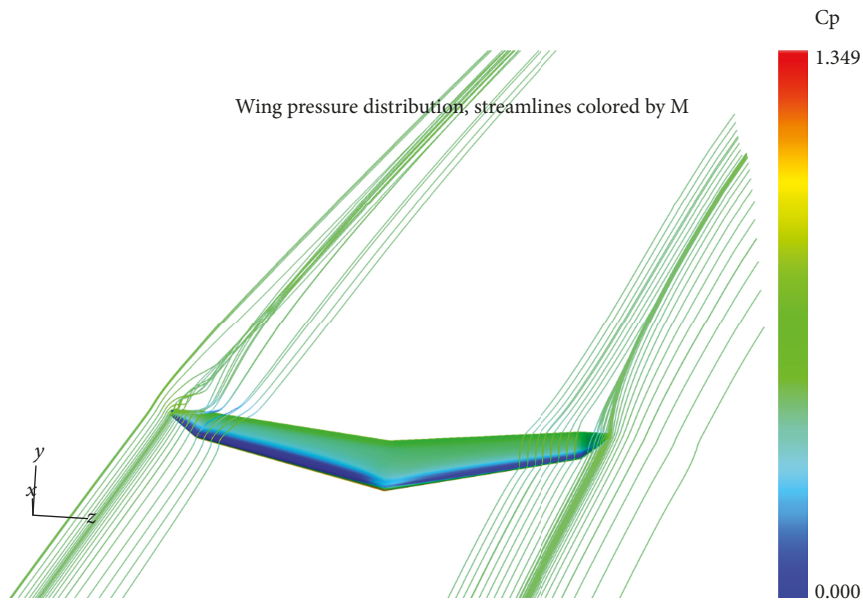


FIGURE 15: BGK wing with folding wing tip at SW1.

Figure 22. For the 3D mesh on the complete aircraft model (rather than the reflection plane model), the mesh about the reflection plane is simply copied over towards the other side. The reflection plane then simply becomes a contiguous boundary between the two halves of the complete model. For each wing surface then, there were 53 span wise points on the solid wing surface and 24 points from the wing tip to the far spanwise boundary. In the chordwise sense, the wing stretched from the trailing edge at point 32 on the lower surface towards the leading edge and back to the trailing edge at chord point 134. The first 31 points were thus reserved for the wake. Normal to the wing, the mesh traversed fine grid at the surface and stretched and curved towards the reflection plane boundary. The fuselage stretched from point 15 on the lower surface to point 151 on the top surface. The first 15 points in each direction described the model support. The

50 azimuthal points at the wing surface would then expand towards the far normal boundary.

The pressure distribution results from computations carried out under flow conditions, $M = 0.8027$, $\alpha = 2.873^\circ$, and $Re/m = 13 \times 10^6$, for the ARA M100 model are shown in Figure 23(a). The convergence history for the computation in Figure 23(b) shows the solution converged by at least two orders of magnitude. The model sting support has been removed from the solutions. More detailed comparisons of the pressure distribution on the wing surface for at least two wing locations are shown in Figure 24. Figure 24(a) captures the pressure distribution at location $\eta = 0.198$, and Figure 24(b) shows the C_p distribution at $\eta = 0.325$. It is evident that the algorithm performs quite well in being able to resolve the pressure loads on the ARA M100 model. Since the side shear winds are usually encountered close to the

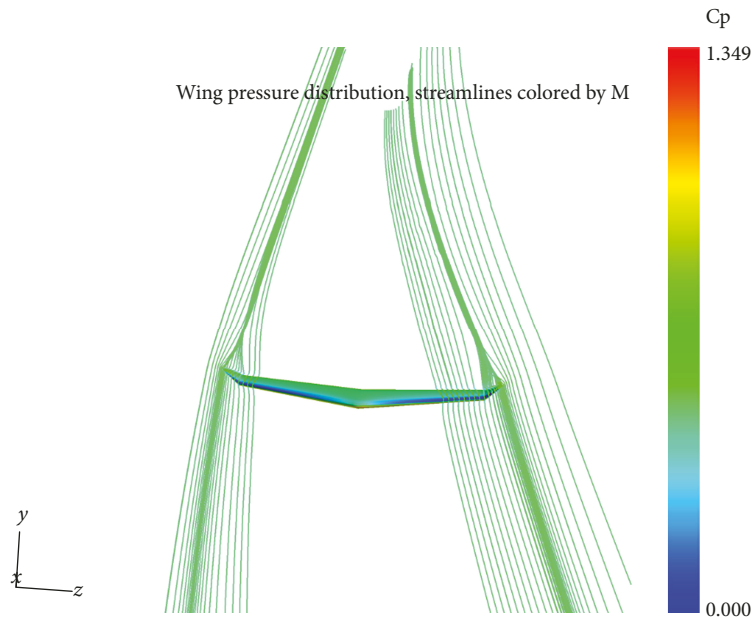


FIGURE 16: BGK wing with folding tip at SW2.

TABLE 2: Lift and drag coefficients with and without folding tips.

	BGK 3D plain wing			BGK 3D wing with folding tip		
	C_L	C_D	C_L/C_D	C_L	C_D	C_L/C_D
No shear	0.6299	0.03804	16.404	0.7133	0.0389	18.337
SW1	0.6478	0.03501	18.503	0.8891	0.02458	36.172
SW2	0.5918	0.03899	15.178	0.7263	0.03931	18.48

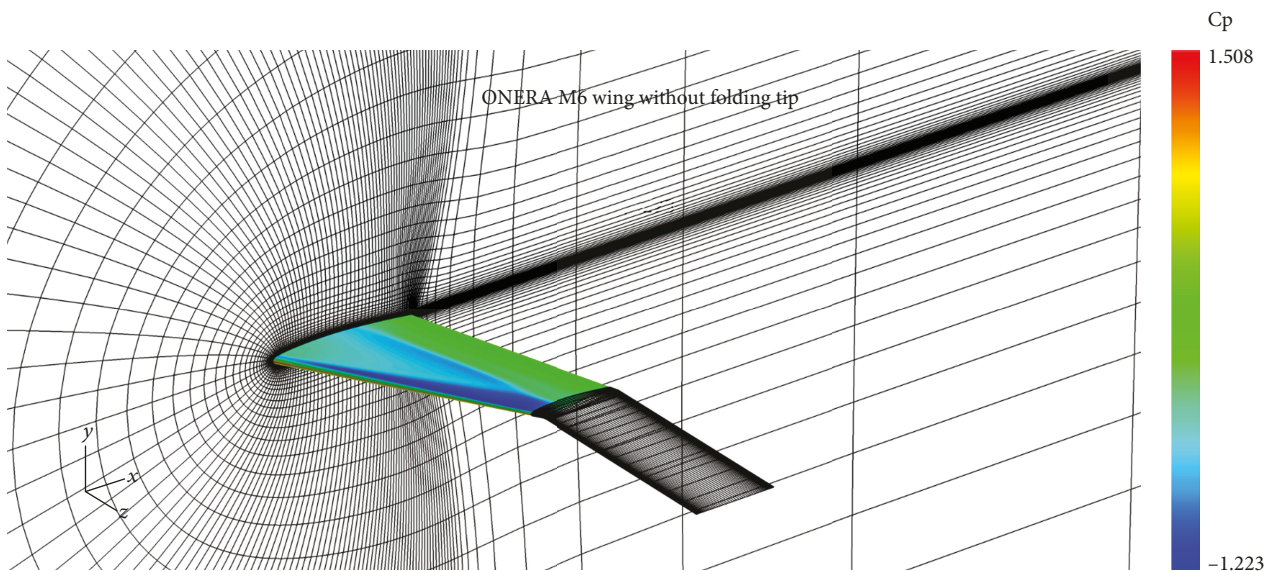


FIGURE 17: ONERA M6 wing shown in the computational mesh ($163 \times 39 \times 65$).

take-off and landing phases of the flight schedule, it is important to compute another flow at a lower Mach number of $M = 0.6$, $\alpha = 1.733^\circ$, and $Re/m = 13 \times 10^6$. The solution from

such execution is shown in Figure 25. It is apparent that the top surface at this lower Mach number condition $M = 0.6$ does not support as much low pressure flow as compared

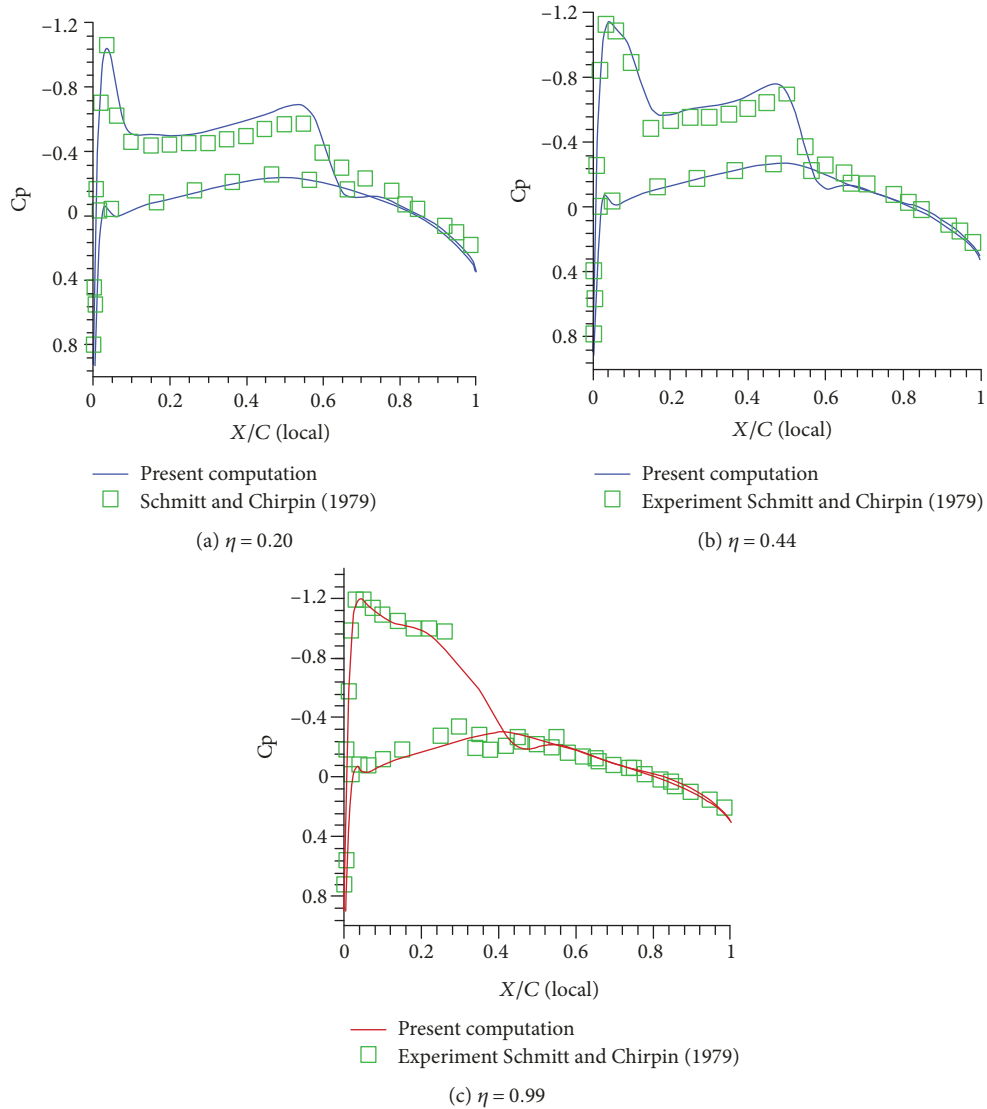
FIGURE 18: Pressure distribution on the ONERA M6 wing at station $\eta = 0.2, 0.44,$ and 0.99 .

TABLE 3: Lift and drag coefficients on the ONERA M6 plain wing.

	C_L	C_D	C_L/C_D
Le Moigne [22]	0.2697	0.01763	15.29
Neilsen and Anderson [23]	0.2530	0.01680	15.06
Lee et al. [24]	0.2622	0.01751	14.97
Present computations	0.2712	0.01610	16.84

to the solution at $M = 0.8027$. The shock from the flow at $M = 0.8027$ also is much stronger which can lead to earlier flow separation. The shock in the case of a low Mach number flow $M = 0.6$ is weaker and much smeared. It must also be noted that for this case, the experiment was carried out with a transition strip which traversed almost entirely across the semispan whereas the present computations were conducted for a completely turbulent flow, and thus, in the strict sense, the detailed pressure distribution comparisons would not be

too useful. Overall load coefficients should in both cases be quite reasonable.

The lift and drag coefficients are compared against the experimental data in Table 5. It is evident that for the lower Mach number case, the fully turbulent wing generated smaller lift when compared to the experiment conducted with a transition strip.

A side shear flow was now applied to the ARA M100 wing-fuselage configurations with flight conditions at $M = 0.6$, $\alpha = 1.733^\circ$, and $Re/m = 13 \times 10^6$. The side shear wing varies from a maximum of 3x the forward velocity, 4 m above the wing plane, reducing to a zero velocity at the wing plane and then increasing negatively to 3x the forward velocity at 4 m below the wing plane. The wind shear is captured at the far starboard boundary in Figure 26.

The ARA M100 wing-fuselage model was computed with and without side wind shear. Both results are shown in Figure 27. It is clear from the surface pressure distribution in the two cases that the presence of fuselage has

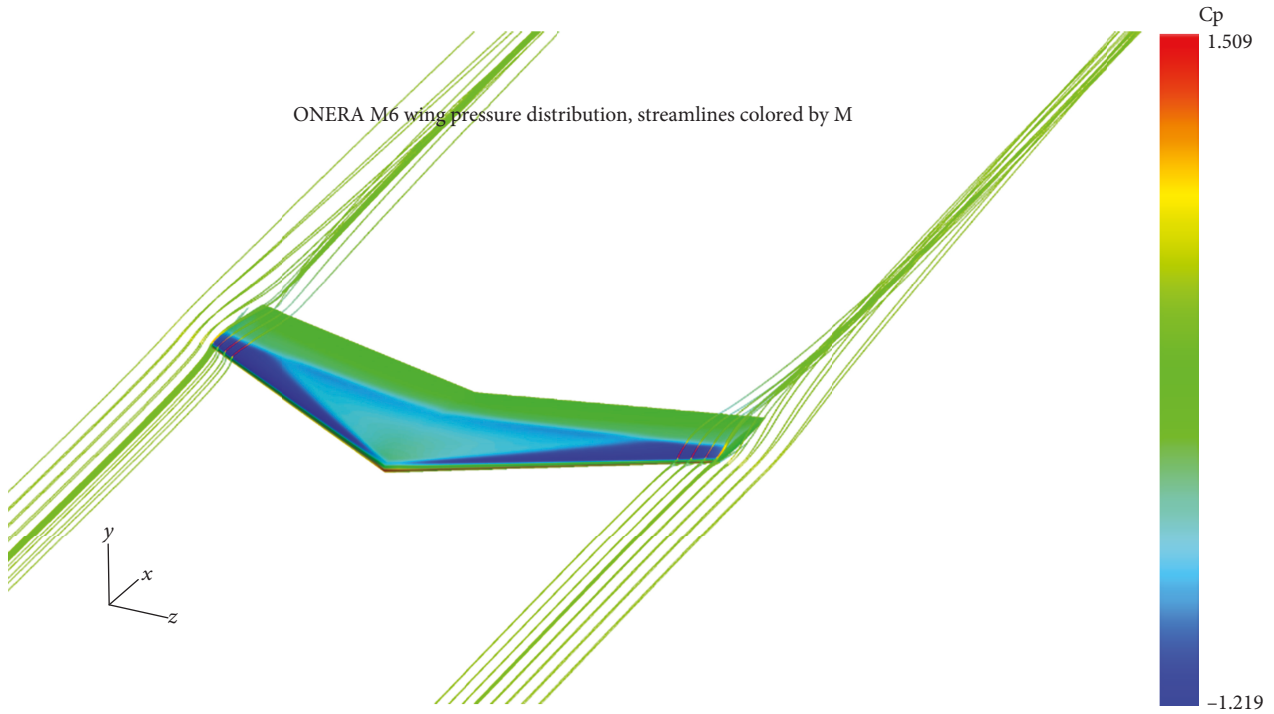


FIGURE 19: Plain ONERA M6 wing under SW1.

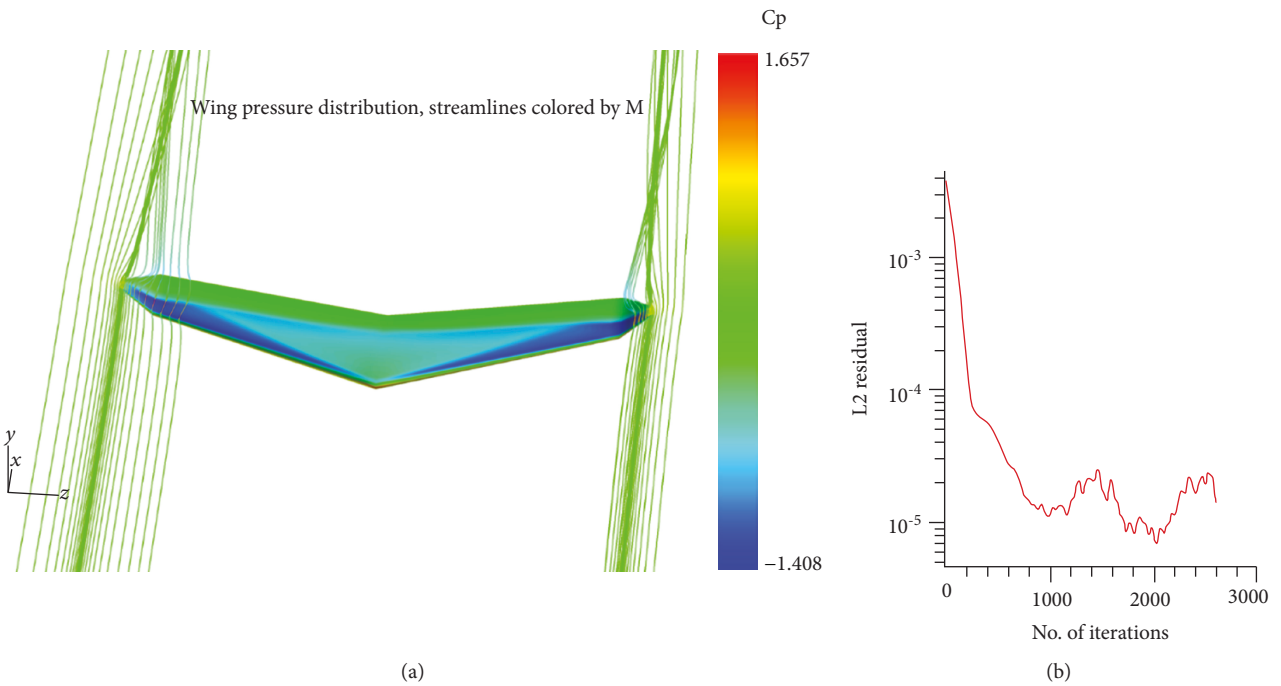


FIGURE 20: ONERA M6 wing with folding tip under SW1.

TABLE 4: Lift and drag coefficients of the ONERA M6 wing with and without folding tips.

	C_L	C_D	C_L/C_D
Present computations	0.2712	0.01610	16.84
Plain ONERA M6 wing under SW1	0.3225	0.01712	18.83
ONERA M6 wing with folding tips	0.3773	0.01912	19.73

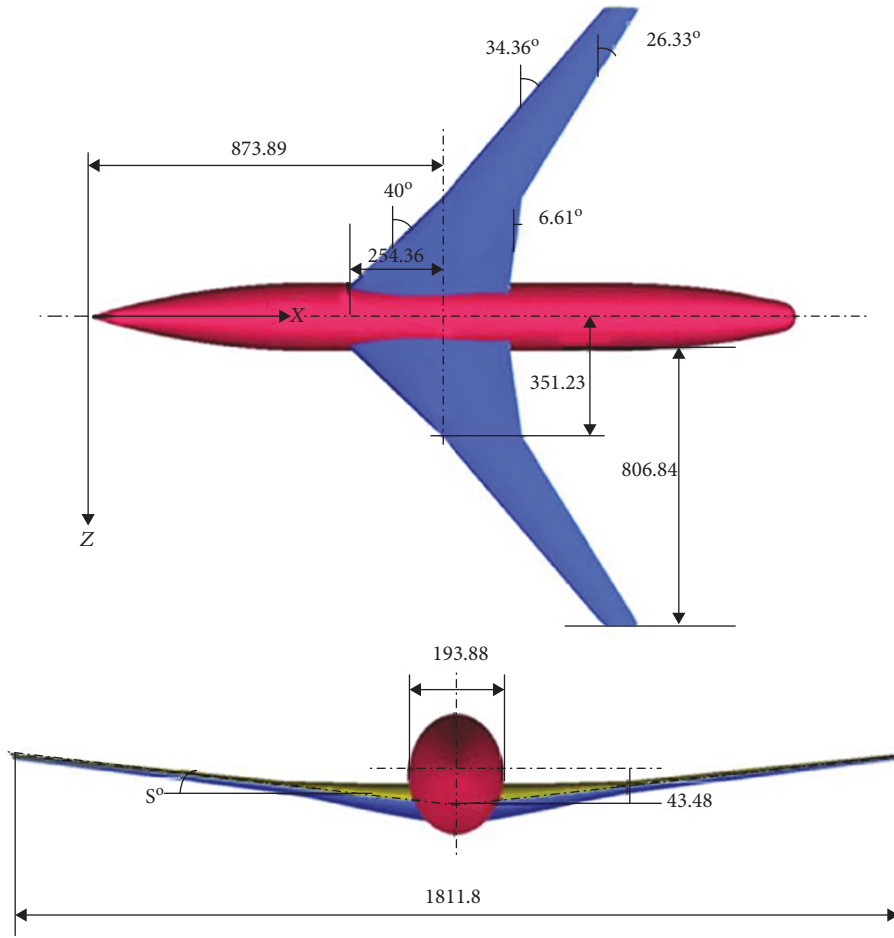


FIGURE 21: Basic dimension of the ARA M100 wing-fuselage model, Carr and Pallister [13].

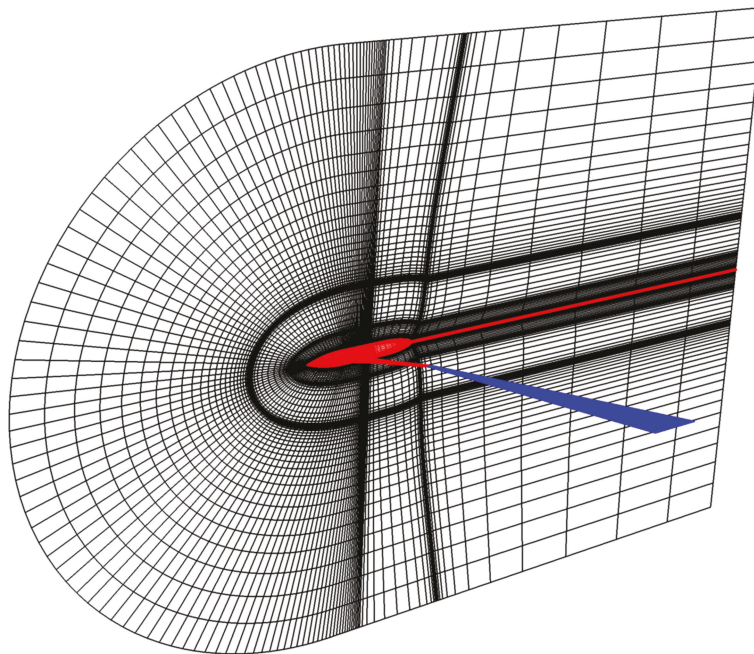


FIGURE 22: A C-H mesh having dimensions (165 × 50 × 85) showing the reflection plane version of the ARA M100 wing-fuselage model.

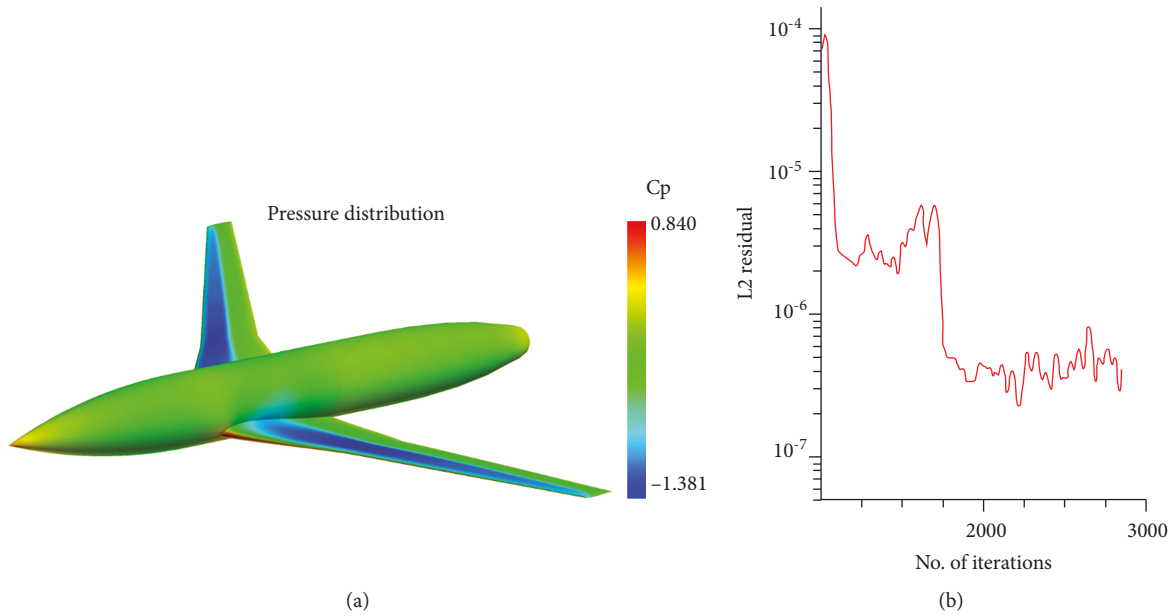


FIGURE 23: C_p distribution on ARA M100 wing-fuselage configuration. $M = 0.8027$, $\alpha = 2.873^\circ$, and $Re/m = 13 \times 10^6$ (a); convergence history (b).

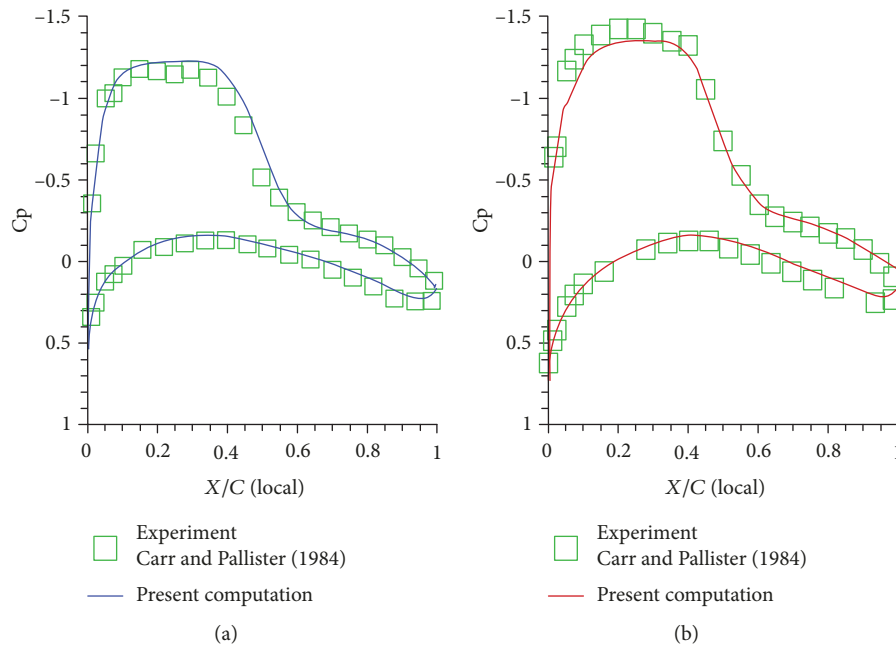


FIGURE 24: C_p distribution on ARA M100 wing-fuselage configuration. $M = 0.8027$, $\alpha = 2.873^\circ$, and $Re/m = 13 \times 10^6$. $\eta = 0.198$ (a); $\eta = 0.325$ (b).

profound influence on the immediate aerodynamics in close vicinity of the aircraft. The streamlines too appear to be affected by the side wind shear. When no side shear is present, the streamlines placed near the wing tip traverse past the wing eventlessly.

It is seen that very close to the tip itself, they rope around the tip and process downstream smoothly. However, there is much bending of the streamlines close to

the wing tip, under side shear wind. Some streamline traces simply get dragged into the low pressure region and are captured to stay very close to the surface before being released into the wake. The absolute lifting loads on the aircraft are much reduced by the side wind shear. Comparison of various lift and drag coefficient between flow conditions with and without side shear is contained in Table 5.

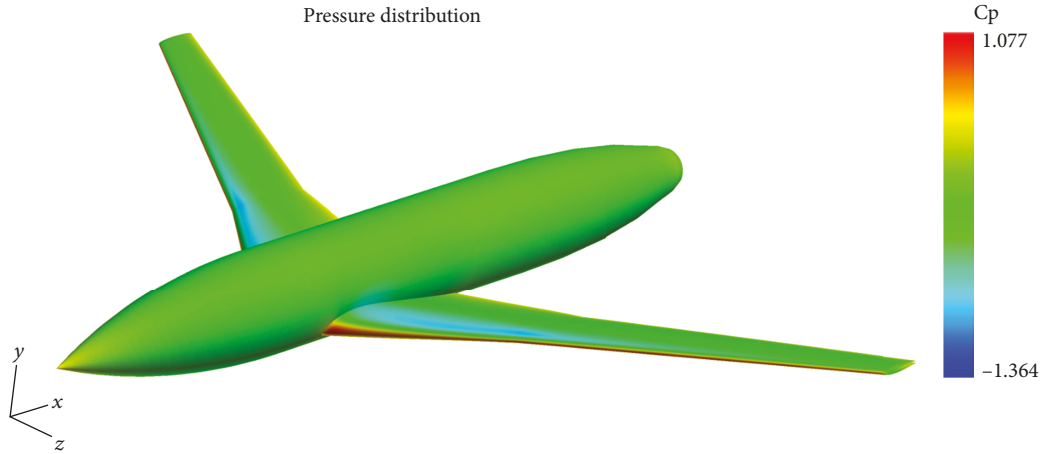


FIGURE 25: Cp distribution on ARA M100 wing-fuselage configuration. $M = 0.6$, $\alpha = 1.733^\circ$, and $Re/m = 13 \times 10^6$.

TABLE 5: Lift and drag coefficients on ARA M100, with and without side shear wind.

	C_L	C_D	C_L/C_D
Computation: $M = 0.6$, $\alpha = 1.733^\circ$, and $Re/m = 13 \times 10^6$ (no side shear wind)	0.3338	0.0257	12.988
*Experiment: $M = 0.6$, $\alpha = 1.733^\circ$, and $Re/m = 13 \times 10^6$	0.4199	0.02239	18.75
Computation: $M = 0.6$, $\alpha = 1.733^\circ$, and $Re/m = 13 \times 10^6$ (with side shear wind)	0.0155	0.05541	0.2797

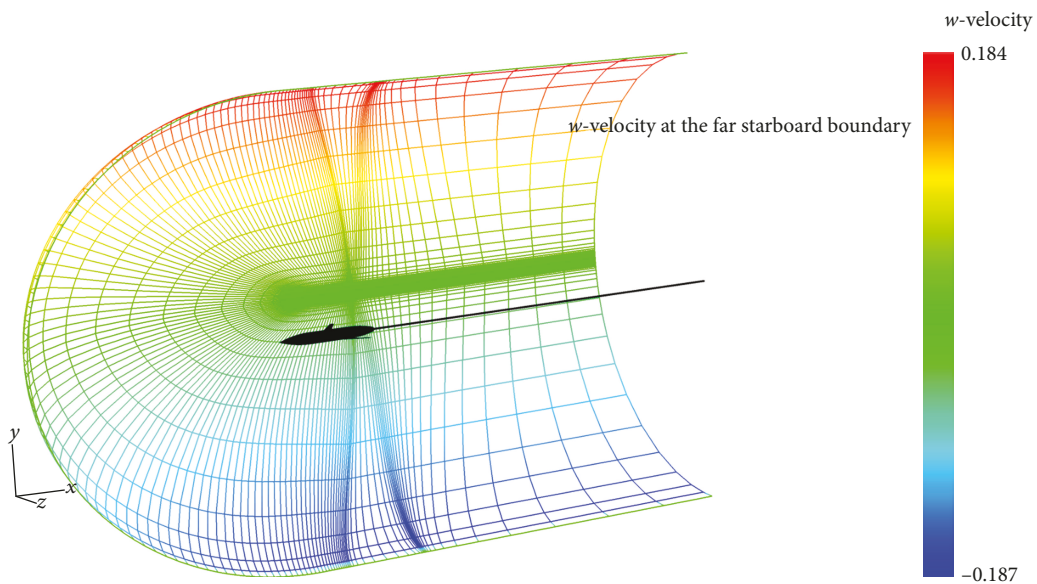


FIGURE 26: Side wind shear showing w -velocity components at the far starboard boundary.

It appears that lift is totally devastated by the application of the side shear wind, whereas the drag too has more than doubled when compared to no side shear. The same case has been studied earlier for the ONERA M6 wing with and without folding tips as well as a conceptual BGK airfoil-based swept wing, again with and without folding tips. It appears that the effects from the presence of a fuselage are far more consequential than simple wings with or without

folding tips. The aircraft would not remain airborne under such shear loads.

5. Conclusion

Several aircraft configurations from simple wings to wings with folding tips and wings with a fuselage were investigated

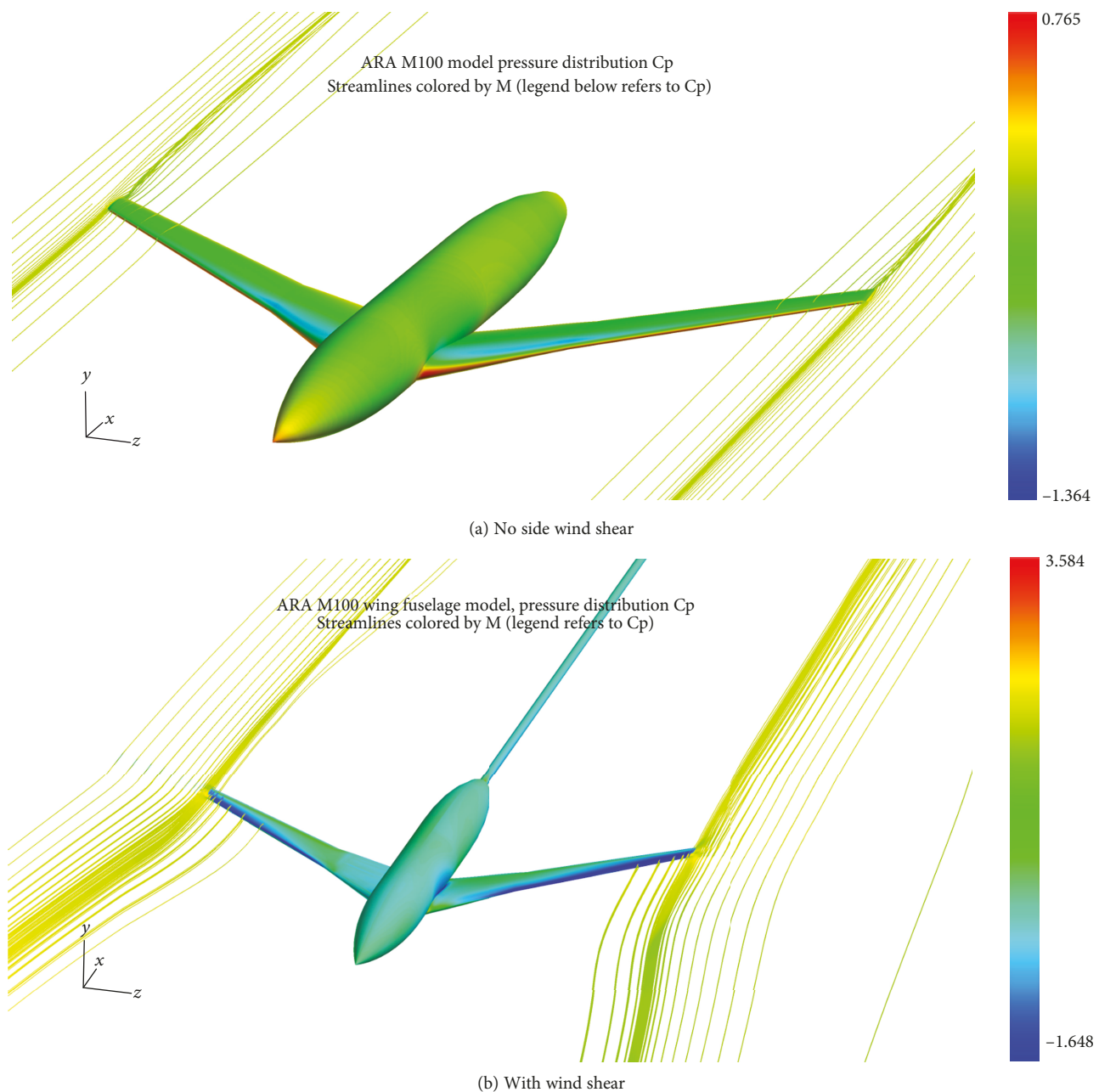


FIGURE 27: C_p distribution and wing tip streamlines on ARA M100 wing-fuselage configuration. $M = 0.6$, $\alpha = 1.733^\circ$, and $Re/m = 13 \times 10^6$; (a) without side wind shear and (b) wing wind shear.

for the effects of simple side wind shear on the aerodynamic performance.

It appears that simple wing shapes with no-fuselage or folding wing tips were not too severely affected by the simple side wind shear. However, aircraft wings with folding wing tips or winglets responded quite vigorously with a noticeable increase in the wing lift coefficient.

An aircraft with a fuselage however suffered from noticeable loss of lift coupled with an increase of drag when a side shear wind was applied in the presence of a normal flight.

The model investigated thus far only focussed on a simple side shear wing model. It might not capture the entire picture of performance deterioration from a more sophisticated

shear model which would include wind shear effects from lateral velocity changes or sinusoidal variation of velocities in parallel with the above results.

Data Availability

The computational data used to support the findings of this study are available from the corresponding author upon request.

Conflicts of Interest

The author declares that there is no conflict of interest regarding the publication of this paper.

Acknowledgments

This work was funded by the Deanship of Scientific Research (DSR), King Abdulaziz University, Jeddah, under grant No. 135-173-D1440. The author, therefore, acknowledges with thanks the DSR technical and financial support.

References

- [1] J National Aeronautics and Space Administration, Langley Research Center, *Making the skies safer from wind shear*, 1992, Archived from the original on March 29, 2010, <https://www.nasa.gov/centers/langley/news/factsheets/Windshear.html>.
- [2] R. L. Bowles, "Reducing wind shear risk through airborne systems technology," in *17th ICAS Congress*, Stockholm, Sweden, September 1990.
- [3] D. A. Hinton, *Piloted-simulation evaluation of recovery guidance for microburst wind shear encounters*, NASA TP 2886, Washington, DC, USA, 1989.
- [4] W. Frost, "Flight in Low-Level Wind Shear," NASA CR-3678, George C. Marshall Space Flight Center, Washington, DC, USA, 1983.
- [5] T. T. Fujita and R. M. Wakimoto, "Five scales of airflow associated with a series of downbursts," *Journal of Monthly Weather Review*, vol. 109, no. 7, pp. 1438–1456, 1981.
- [6] S. S. Mulgund and R. F. Stengel, "Aircraft flight control in wind shear using sequential dynamic inversion," *Journal of Guidance, Control, and Dynamics*, vol. 18, no. 5, pp. 1084–1091, 1995.
- [7] A. Jameson and M. Fatica, *Using computational fluid dynamics for aerodynamics*, Stanford University, Stanford, CA, USA, 2001, http://aero-comlab.stanford.edu/fatica/papers/jameson_fatica_hpc.pdf.
- [8] P. Moin and K. Kim, "Tackling turbulence with supercomputers," *Scientific American*, vol. 276, no. 1, pp. 62–68, 1997.
- [9] P. R. Spalart, W.-H. Jou, M. Strelets, and S. R. Allmaras, "Comments on the feasibility of LES for wings, and on a hybrid RANS/LES approach," in *First AFOSR International Conference on DNS/LES*, Ruston, LA, USA, August 1997 (In "Advances in DNS/LES," C. Liu & Z. Liu Eds., Greyden Press, Columbus, OH).
- [10] M. J. Piosenski, D. J. Jones, M. Mokry, and L. H. Ohman, "Supplementary investigation of the BGK no. 1 airfoil; wall interference study," NRC, LTR-HA-5X5/0127, Ottawa, Canada, 1981.
- [11] N. Sudani, H. Kanda, and H. Miwa, *A comparative study of BGK airfoil no. 1 data in high Reynolds number transonic wind tunnel*, NAL Report, NAL-TR-1911T, Japan, 1993.
- [12] V. Schmitt and F. Charpin, *Pressure distributions on the ONERAM6- wing at transonic Mach numbers*, AGARD AR-138, 1979.
- [13] M. P. Carr and K. C. Pallister, *Pressure distributions measured on Research Wing M100 mounted on an axisymmetric body*, AGARD AR-138, 1989.
- [14] M. Vinokur, "Conservation equations of gas dynamics in curvilinear coordinate system," *Journal of Computational Physics*, vol. 14, no. 2, pp. 105–125, 1974.
- [15] R. Beam and R. F. Warming, "An implicit finite difference algorithm for hyperbolic system in conservation law form," *Journal of Computational Physics*, vol. 22, no. 1, pp. 87–110, 1976.
- [16] T. H. Pulliam and D. S. Chaussee, "A diagonal form of an implicit approximate-factorization algorithm," *Journal of Computational Physics*, vol. 39, no. 2, pp. 347–363, 1981.
- [17] B. S. Baldwin and T. J. Barth, *A one-equation turbulence transport model for high Reynolds number wall-bounded flows*, NASA Technical Memorandum 102847, 1990.
- [18] P. R. Spalart and S. R. Allmaras, "A one-equation turbulence model for aerodynamic flows," *La Recherche Aérosptiale*, no. 1, pp. 5–21, 1994.
- [19] F. Homann, "Der Einfluß großer Zähigkeit bei der Strömung um den Zylinder und um die Kugel," *ZAMM - Zeitschrift für Angewandte Mathematik und Mechanik*, vol. 16, no. 3, pp. 153–164, 1936.
- [20] "Wind Shear" – FAA-P-8740-49 AFS-8, Federal Aviation Administration, 2008, HQ 101130.
- [21] N. Durrani and N. Qin, "Comparison of RANS, DES and DDES results for ONERA M-6 Wing at transonic flow speed using an in-house parallel code," in *49th AIAA Aerospace Sciences Meeting including the New Horizons Forum and Aerospace Exposition*, Orlando, FL, USA, January 2011.
- [22] A. Le Moigne, *A discrete Navier-Stokes adjoint method for aerodynamic optimization of blended wing-body configurations*, [Ph.D. thesis], Cranfield University, UK, 2002.
- [23] E. J. Neilsen and W. L. Anderson, "Recent improvements in aerodynamic design optimization on unstructured meshes," in *39th Aerospace Sciences Meeting and Exhibit*, Reno, NV, USA, January 2001.
- [24] J. Lee, C. S. Kim, C. Kim, O. H. Rho, and K. D. Lee, "Parallelized design optimization for transonic wings using aerodynamic sensitivity analysis," in *40th AIAA Aerospace Sciences Meeting & Exhibit*, Reno, NV, USA, January 2002.

